

Experimental and numerical investigation of WEC-type floating breakwaters: A single-pontoon oscillating buoy and a dual-pontoon oscillating water column

Yong Cheng^a, Lei Fu^a, Saishuai Dai^{b,*}, Maurizio Collu^b, Chunyan Ji^a, Zhiming Yuan^{a,b}, Atila Incecik^b

^a School of Naval Architecture and Ocean Engineering, Jiangsu University of Science and Technology, Zhenjiang, 212003, China

^b Naval Architecture, Ocean and Marine Engineering Department, University of Strathclyde, Glasgow, United Kingdom

ARTICLE INFO

Keywords:

Floating breakwater
Wave energy converter
Fluid-structure interaction
Oscillating buoy
Oscillating water column

ABSTRACT

Wave energy converters (WECs) integrated into floating breakwaters or, more generally, their designs also used as wave absorbers can provide a space- and cost-sharing solution to enhance the efficiency of coastal protection. In this study, the hydrodynamic performances of an oscillating buoy (OB)-type single-pontoon floating breakwater (SPFB) and an oscillating water column (OWC)-type dual-pontoon floating breakwaters (DPFB) are evaluated, respectively, and are comprehensively compared with each other. A series of physical experiments were conducted to investigate the effects of wave parameters, geometrical dimensions, gap distances and PTO damping coefficients. Numerical simulations based on the fully nonlinear potential flow theory cross-check the measured data, and help to further understand the contribution of higher-order waves. It is found that both the wave attenuation and energy conversion of the OWC-type DPFB with a non-uniform draft (i.e. shallow front-pontoon draft and deep back-pontoon draft) are better than those of the OB-type SPFB with the same displacement. Meanwhile, for an OWC-type DPFB, a larger ratio of the chamber width and the total pontoon width has a beneficial effect on the wave attenuation, but has an adverse effect on the maximum energy conversion efficiency. Under the premise of the same pontoon draft, the maximum conversion efficiency of the OWC for the optimal opening ratio is higher than that of the OB for the optimal PTO damping, but the effective frequency bandwidth is almost identical between two devices. Strong wave nonlinearity can generate more energy dissipation induced by the viscous effect and the vortices, resulting into the reduction of energy extraction.

1. Introduction

Large-scale blockade caused by the ongoing COVID-19 has contributed to the global economic recombination, and thus some regions have particularly stressed on the reform of energy. Maximizing the utilization of renewable energy is an effective way to achieve clean transition of the energy mix (Zhu et al., 2022). The International Energy Agency (IEA) has reported that power generated by renewable energy will pass 50% of the growth of global power generation by 2035 (International Energy Agency,). Wave energy as one of the main forms of renewable marine energy, has the features of large reserves (total global reserves about 2 TW), high energy flux intensity (up to 3 kW/m²), and wide distribution (Oliveira-Pinto et al., 2020). However, the high Levelised Cost of Electricity (LCOE) described as the holistic cost of generation power impedes

the commercial-scale wave power operations. Integrating wave energy converters (WECs) with floating breakwaters (FBs) provides a promising way to reduce the LCOE due to the cost-sharing and space-sharing strategies. Additionally, the synergistic effect between WECs and FBs can be realized. For example, WECs can absorb part of incident wave energy, enhancing the wave attenuation capacity of FBs. Meanwhile, the scattering waves generated by FBs can be gathered near WECs, boosting energy extraction performance of WECs.

From the perspective of enhancing economic competitiveness and practical engineering applications, FBs should be as maintenance free as possible during the prolonged interaction with incoming waves. Single-pontoon floating breakwaters (SPFBs) and dual-pontoon floating breakwaters (DPFBs) are the most common structures considering the requirements of simple configuration and good durability in design.

* Corresponding author. Naval Architecture, Ocean and Marine Engineering Department, University of Strathclyde, Glasgow, United Kingdom.

E-mail address: saishuai.dai@strath.ac.uk (S. Dai).

<https://doi.org/10.1016/j.coastaleng.2022.104188>

Received 2 April 2022; Received in revised form 17 May 2022; Accepted 16 July 2022

Available online 21 July 2022

0378-3839/© 2022 The Authors. Published by Elsevier B.V. This is an open access article under the CC BY license (<http://creativecommons.org/licenses/by/4.0/>).

Therein, a SPFB is generally regarded as a simple geometric configuration such as rectangular type or cylinder type with a certain draft underwater. The SPFB attenuating surface waves mainly depends on the process of reflection of incident wave and generation of wave breaking. [Diamantoulaki and Angelides \(2010\)](#) compared the hydrodynamic performance between single floating breakwaters with and without hinge. It is found that the structure of the hinged floating breakwater array strongly affects the response and effectiveness of the array. [Chang et al. \(2012\)](#) proposed a V-shaped breakwater and discussed the influence of its parameters on wave height distribution. As a general extension, [Wei et al. \(2013\)](#) carried out a numerical analysis of the nonlinear interactions between water waves and the submerged floating breakwaters. The comparison of the results shows that they are in good agreement in terms of free water surface, tension acting on mooring line and floating body dynamics. Differently from the previous research works, [Chen et al. \(2012\)](#) presented a box-pontoon floating breakwater attaching horizontal plates and studied it under two-dimensional linear potential flow theory, finding that the width of floating breakwater is an important factor affecting the wave transmission coefficient of floating breakwater. In addition, horizontal plates help to reduce wave propagation on floating breakwaters. Along with the resemble line, [Christensen et al. \(2018\)](#) presented a numerical and experimental study on the floating breakwater with wing plates. It was found that attaching porous wing plates on breakwaters can significantly enhance the motion but reduce the transmission and reflection effect. [Liu and Wang \(2020\)](#) presented a coupled hydrodynamic-mooring model based on the smoothed particle hydrodynamics (SPH) to investigate the performance of submerged moored box-type floating breakwaters with different shapes numerically. [Liang et al. \(2022\)](#) carried out scaled experiments on the SPFB with different mooring configurations, showing that the mooring configuration can affect the transmission coefficient in long-period waves.

It is easily understood that the SPFB can be used as an oscillating buoy (OB)-type WEC by installing a power take-off (PTO) system above the original base structure to absorb the kinetic energy of the motions of the SPFB. [Michaelides and Angelides \(2012\)](#) introduced a new type of flexible floating breakwater (FFB). Adjacent floating modules by relative motion to capture wave energy, the results indicated that the horizontal wave can be attenuated by the device to a great extent while realizing the utilization of wave energy. [Ning et al. \(2016a,b\)](#) proposed an integrated system of a pile-constrained floating breakwater as an oscillating-buoy WEC with PTO system vertically. It was found that the energy capture efficiency of the integrated system and wave dissipation performance is related to the parameters of the integrated system. [Chen et al. \(2020\)](#) implemented a viscous-flow model based on incompressible Navier-Stokes (N-S) equations to optimize the geometrical shape of the WEC-type floating breakwater studied by [Ning et al. \(2016a,b\)](#). [Madhi and Yeung \(2018\)](#) adopted a Weakly Compressible Smoothed Particle Hydrodynamics (WCSPH) method to demonstrated the better wave attenuation and wave energy extraction capacity of the floating breakwater with an asymmetrical wedge shape. Similar conclusions were obtained by [Zhang et al. \(2021\)](#), comparing the hydrodynamic performance of symmetric and asymmetric WEC-type floating breakwaters. [Windt et al. \(2021\)](#) simulated the hemispherical OB named as Wavestar ([Kramer et al., 2011](#)) using the two-phase numerical wave tank (NWT) to exploit the high-fidelity capability of computational fluid dynamics (CFD) models.

However, the wave attenuation performance of SPFBs is generally unsatisfactory in long-period waves due to the finite breakwater width. The conventional method to improve the hydrodynamic performance is by increasing the draft or width of the floating breakwater, which requires more construction cost. Another interesting idea is by disassembling a single pontoon into double pontoons with the overall structural mass kept the constant. Thus, the gap is generated between the double pontoons for a DPFB. The design of this configuration is to allow incident waves entering into the gap so that the internal water in the gap

oscillates up and down to lead more wave energy dissipation compared to a SPFB. [Liu and Li \(2014\)](#) applied the matching eigen-function expansion technique combined with linear potential flow theory to examine the gap resonance between two rectangular pontoons. [Tang et al. \(2011\)](#) studied a DPFB equipped with a cage for aquaculture, finding that the mooring forces and motion responses slightly decrease due to the effect of fish net system. Similar design was also proposed by [Ji et al. \(2017\)](#), analyzing the characteristics of a dual cylindrical pontoon-type FB attached with some rows of vertical plane nets. It is demonstrated that the addition of the flexible nets can improve wave attenuation by 10% in long-period waves (prototype wave periods >10 s). Furthermore, [Cebada-Relea et al. \(2022\)](#) numerically simulated five pontoon breakwaters to reveal the fluid-structure interaction among array multi-modular pontoons.

In the aspect of design, the gap between two pontoons can be regarded as an oscillating water column (OWC) where the piston-type motion of the internal water compresses the airflow through a turbine to produce electricity. [Koo \(2009\)](#) proposed an air chamber floating breakwater, which has the characteristics of OWC wave energy device. The hydrodynamic research on this type of structure are analyzed based on nonlinear numerical flume, and revealed that the wave dissipation performance of this type of breakwater is obviously better than that of traditional box breakwater. [He et al. \(2013\)](#) compared experimentally the hydrodynamic difference between FBs with symmetric and asymmetric air chambers, and concluded that the asymmetric configuration of the air chambers can broaden the effective frequency bandwidth extracting wave energy. [He et al. \(2019\)](#) followed up with an analytical study and simulated the hydrodynamic performance of a pile-supported OWC device as a floating breakwater system. [Ning et al. \(2016a,b\)](#) conducted an experiment to investigate the hydrodynamic performance of a fixed OWC, showing that the energy conversion can be enhanced by a larger chamber width in long-period waves. Following this study, [Ning et al. \(2019\)](#) investigated experimentally the hydrodynamics of a land-based dual-chamber OWC (the chambers were located along the wave propagating direction). Furthermore, [Ning et al. \(2017\)](#) investigated the power extraction performance of a cylindrical dual-chamber OWC. This study concluded that the power conversion efficiency increases with increasing the inner-chamber draft or decreasing the outer-chamber draft. [Elhanafi et al. \(2018\)](#) developed a numerical wave tank based on the N-S equations to study the effect of chamber lip draught, chamber width and PTO damping on the performance of single-chamber and dual-chamber OWC devices. [Correia et al. \(2016\)](#) studied experimentally the motion characteristic of an array inter-connected triangular configuration of three OWC spar-buoy devices. [Howe et al. \(2020\)](#) performed an experimental test on the wave attenuation performance of a floating breakwater with array OWC configuration. The OWC system was installed in the front of the breakwater with a parallel arrangement scheme. The results indicated that the hydrodynamic interaction among multiple OWC chambers affected the variation of the transmission coefficient with period. [Guo et al. \(2021\)](#) also proposed a novel OWC-type breakwater integrated system which is attached to a front wall oscillating in the pitch by a torsional spring. It is illustrated that the energy conversion efficiency is strongly related to the motion response of the front wall. [Pawitan et al. \(2019\)](#) integrated a caisson type OWC-WEC into a vertical breakwater, showing that the internal water motion can reduce wave loads on the caisson breakwater. [Zheng et al. \(2019\)](#) adopted the eigenfunction matching method based on linear potential flow theory to investigate the hydrodynamic performance of multiple coast-integrated OWCs. [Wang et al. \(2022\)](#) mainly studied the hydrodynamic characteristics of the narrow gap between a heaving OWC and a floating stationary breakwater. Through the optimization of the gap distance, the conversion efficiency can be effectively amplified at the resonant frequency.

It is not possible to infer the difference on the hydrodynamic performance between the OB-type and OWC-type FBs from the published studies. The motivation and novelty of this paper is twofold: firstly to

consider different WEC-type floating breakwaters including an OB-type SPFB and an OWC-type DPFB with the same displacement i.e. mass, and secondly to investigate systematically both the wave attenuation and the energy extraction performance of the two devices through a series of experimental tests. This will help to optimize the configuration of WEC-breakwater integration that achieves cost-sharing and space-sharing WEC-breakwater solutions.

The paper is organized as follows: firstly, the description of the experimental setup and method involved in the data analysis are given in Section 2. Section 3 establishes a numerical wave tank based on the N-S equations to further cross-check experimental data. In Section 4, the parametric sensitivity analysis is described firstly. Then the detailed comparisons between the two WEC-type floating breakwaters discussed. Finally, the conclusions obtained from this study are summarized in Section 5.

2. Experiments

2.1. Experimental setup

The experiments were conducted in a 40 m long, 0.8 m wide, 1.4 m deep wave flume at the Jiangsu University of Science and Technology, China. A piston-type wave-maker is located at one end of the wave flume to generate incident waves. A slope-type wave beach is arranged at the other end of the flume to absorb the transmitted waves. The model scale is set as 1:20 based on the Froude scaling principle. In the present study, an OB-type SPFB and an OWC-type DPFB are considered with length $L = 0.78$ m perpendicular to the incoming wave direction, respectively. In order to compare the hydrodynamics of the OB-type SPFB and the OWC-type DPFB, the displacements and the total pontoon widths are kept the same for the two devices. Here, the OB-type SPFB model performed only heave motion while the OWC-type DPFB model is fixed on the free water surface.

These models were manufactured from 10 mm thick Perspex sheets. The details of the two scaled models are given in Tables 1 and 2, and supported by Fig. 1 (a) and (b). The OB-type SPFB model was restrained by two slide rails. Each slide rail is made of a linear guide and a sliding block, and the friction coefficient is about 0.03 and thus its effect on the FB motion is negligible. The PTO system of the OB-type SPFB is modeled by an aerodynamic damper which consists of a tunable nozzle, an air cylinder and a piston rod. The PTO damping load is generated by the reciprocating motion of the piston rod in the cylinder, and is adjusted by tuning the nozzle at the damper. A tension sensor was bonded on the SPFB and the end of the piston rod to record the PTO damping load. Three different PTO damping coefficients ($b_{pto} = 40$ N/m, 150 N/m and 300 N/m) are set by fitting the relationship between the damping load and the FB motion measured by a non-contact optical Qualysis tracking system. It is demonstrated by Zhang et al. (2021) that the transmission coefficient of the SPFB is greatly dependent on the body draft. Thus, three sets of body drafts (i.e. $d_s = 0.10$ m, 0.15 m and 0.20 m) are considered with the fixed FB width $b_s = 0.3$ m. These model drafts are adjusted by using the customized steel ballast. The ballasts were fixed at the bottom of the model to prevent the ballast from moving during measurement and assure the required accuracy.

The OWC-type DPFB model is fixed by six vertical steel frames

Table 1
Physical parameters of the OB-type SPFB models.

Pontoon Length (m)	Pontoon width (m)	Pontoon draft (m)	PTO damping (Ns/m)
0.78	0.3	0.10	150
0.78	0.3	0.15	150
0.78	0.3	0.20	150
0.78	0.3	0.15	40
0.78	0.3	0.15	300

Table 2
Physical parameters of the OWC-type DPFB models.

Pontoon Length (m)	Pontoon width (m)	Front-pontoon draft (m)	Back-pontoon draft (m)	Chamber width (m)	Opening ratio (%)
0.78	0.15	0.10	0.10	0.25	0.769
0.78	0.15	0.15	0.15	0.25	0.769
0.78	0.15	0.20	0.20	0.25	0.769
0.78	0.15	0.10	0.20	0.25	0.769
0.78	0.15	0.15	0.20	0.25	0.769
0.78	0.15	0.10	0.15	0.25	0.769
0.78	0.15	0.15	0.15	0.15	0.769
0.78	0.15	0.15	0.15	0.35	0.769
0.78	0.15	0.10	0.15	0.25	0.393
0.78	0.15	0.10	0.15	0.25	1.272

clamped to the flume sides. The widths of the two pontoons are constant $b_d = 0.15$ m which means that the total width of the two pontoons are equivalent to the width of the SPFB. Six sets of pontoon drafts ($d_1 = d_2 = 0.1$ m, $d_1 = d_2 = 0.15$ m, $d_1 = d_2 = 0.20$ m, $d_1 = 0.1$ m and $d_2 = 0.20$ m, $d_1 = 0.15$ m and $d_2 = 0.20$ m, $d_1 = 0.1$ m and $d_2 = 0.15$ m, where d_1 and d_2 denote the drafts of the front and back pontoon, respectively) are examined with the pontoon height above the water surface kept constant $h_o = 0.2$ m. Three widths of the OWC chamber are considered (i.e. $b_o = 0.15$ m, 0.25 m and 0.35 m) by changing the gap distance between two pontoons. An orifice located on the roof of the OWC chamber is designed to model the PTO system of the OWC. Three opening ratios which are defined as the ratio of the orifice area A_o and the chamber cross-sectional area A_w are selected (i.e. $\alpha = 0.393\%$, 0.769% and 1.272%) to investigate the effects of the PTO system for the OWC.

The experimental setup of the two WEC-type FBs is shown in Fig. 2 (a) and (b), in which these scaled models were placed 20 m away from the wave-maker. Some wave gauges with a resolution of 0.01 cm were deployed to obtain the wave elevation. For example, two wave gauges (WG1 and WG2) were located upstream from FBs to separate the reflected wave height H_r by using the two-point method (Goda and Suzuki, 1976). One wave gauge (WG3) was located downstream from FBs to calculate the transmitted wave height H_t . Brendmo et al. (1996) reported that when wavelength is long related to the horizontal dimension in the chamber, surface motion at one point can denote the whole surface variation in the chamber. In the present paper, the horizontal dimension inside the chamber is small compared to the prevailing wavelength. The water surface motion in the OWC chamber is measured by WG4. The pneumatic air pressure induced by the water motion in the OWC chamber is recorded by two pressure gauges (PG1 and PG2). The averaged pressure of the two pressure gauges i.e. $p_a = (p_{g1} + p_{g2})/2$ is selected to solve the wave energy extraction from the OWC. A range of regular wave conditions were generated to simulate scaled physical wave conditions. In order to discern the nonlinear wave effect on the hydrodynamic performance of FBs, three different wave heights of $H_i = 0.05$ m, 0.10 m and 0.15 m are considered to cover whole period range from $T = 0.8$ s–2.1 s, where the water depth $h = 1.0$ m is fixed. The detailed wave parameters are listed in Table 3.

In order to minimize the experimental errors, the measurement for each wave case was repeated at least twice. The time history of the tested data was analyzed in the regular oscillatory phase of the experiment. It is found by Ning et al. (2019) that a relatively long time window should be provided to ensure that the experimental data is not contaminated by the re-reflected waves from the wavemaker. Thus, each wave test was completed based on the data collected by the WG 3 covering a time interval of 10 wave periods. The wave elevations at each wave gauge were compared for the repeated tests.

2.2. Data analysis

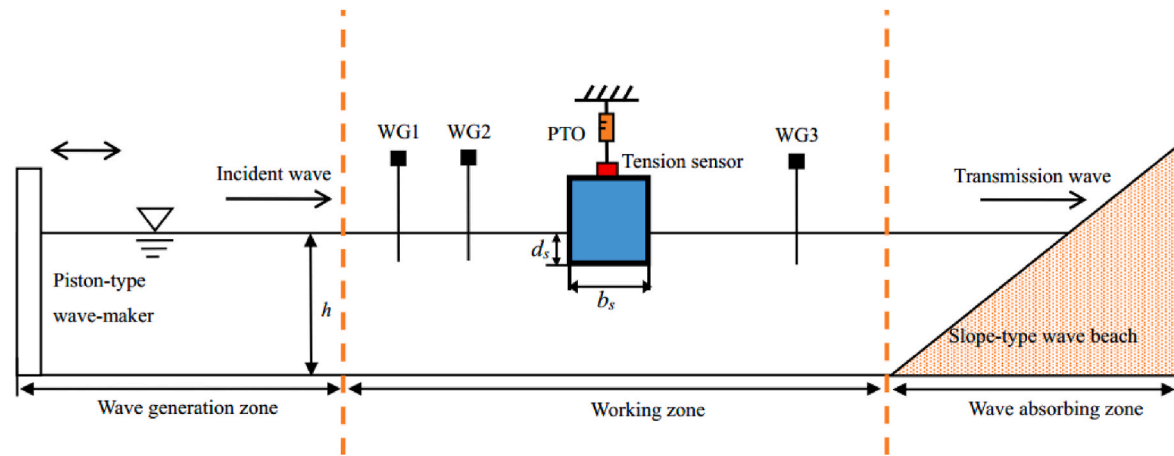
According to the reflected and transmitted wave heights obtained from wave gauges, the wave attenuation capacity of FBs can be denoted



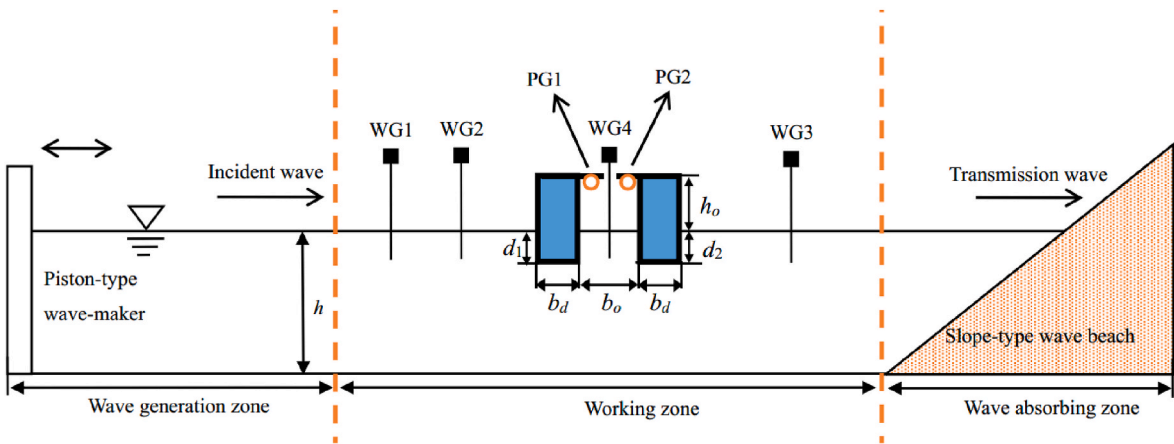
(a) An OB-type SPFB

(b) An OWC-type DPFB

Fig. 1. Photos of the WEC-type floating breakwaters system.



(a) An OB-type SPFB



(b) An OWC-type DPFB

Fig. 2. Schematic of the experimental setup for the WEC-type floating breakwater systems.

as

$$K_t = \frac{H_t}{H_i}$$

$$K_r = \frac{H_r}{H_i} \tag{2}$$

where K_r and K_t denote the reflection coefficient and the transmission coefficient, respectively.

Table 3
Wave parameters in experiments.

Water depth (m)	Wave height (m)	Wave period (s)
1.0	0.05	0.8, 1.0, 1.15, 1.3, 1.5, 1.8, 2.1
1.0	0.10	0.8, 1.0, 1.15, 1.3, 1.5, 1.8, 2.1
1.0	0.15	0.8, 1.0, 1.15, 1.3, 1.5, 1.8, 2.1

The wave coefficient C_η in the OWC chamber is defined as

$$C_\eta = \frac{H_o}{H_i} \quad (3)$$

where H_o is the wave height in the OWC chamber and is measured by WG4.

The heave motion performance for the OB-type SPFB can be denoted by a response amplitude operator (RAO) as

$$RAO = \frac{2\zeta_o}{H_i} \quad (4)$$

where ζ is the heave response of the OB-type SPFB and the subscript 0 denotes the response amplitude.

Based on the working principle of the OB-type SPFB, the heave motion of the FB is absorbed by the aerodynamic damper, and thus the extracted wave power $E_{p(OB)}$ can be defined by averaging data with a time interval of n wave periods (i.e. $t = 5 T-15 T$) as follows

$$E_{p(OB)} = \frac{1}{nT} \int_t^{t+nT} b_{p10} \dot{\zeta}^2 dt \quad (5)$$

where $\dot{\zeta}$ is the heave velocity of the OB-type SPFB.

The average power $E_{p(OWC)}$ generated by the OWC-type DPFB is calculated from the measured pneumatic pressure and wave elevation in the chamber, i.e.

$$E_{p(OWC)} = \frac{A_w}{nT} \int_t^{t+nT} p_a(t) \frac{d\eta(t)}{dt} dt \quad (6)$$

where $d\eta/dt$ is the first-order time derivative of the water surface elevation at location WG4.

The incident wave energy per unit wave front is calculated based on the input mechanism of wave energy flux

$$E_w = \frac{1}{8} \rho_w g H_i^2 c_g \quad (7)$$

where ρ_w and g are the water density and the gravity acceleration, respectively. c_g is the moving velocity of wave group, and is determined by

$$c_g = \frac{\omega}{2k} \left(1 + \frac{2kh}{\sinh 2kh} \right) \quad (8)$$

where ω is the wave frequency. k is the wave number which satisfies the following dispersion relationship

$$\omega^2 = gk \tanh(kh) \quad (9)$$

The energy conversion efficiency of the two WEC-type FBs can be written, respectively as

$$R_{OB} = \frac{E_{p(OB)}}{E_w \cdot L} \quad (10)$$

$$R_{OWC} = \frac{E_{p(OWC)}}{E_w \cdot L} \quad (11)$$

where R_{OB} and R_{OWC} are the energy conversion efficiency of the OB and the OWC, respectively.

3. Numerical comparison with experiments

A fully nonlinear numerical model is developed to compare the experimental results of the two type WEC-FB hybrid systems described above. The numerical model is based on the potential flow theory with a mixed Eulerian-Lagrangian(MEL) time-marching technique. Hydrodynamic loads are accurately calculated using some auxiliary functions. Two linear models for PTO systems of the OB and OWC devices are included in the structural and water motion equations, respectively. The solving process is briefly summarized in the following section.

3.1. Numerical model

In order to involve more general cases, a floating DPFB with an OWC chamber is considered to interact with surface waves, as shown in Fig. 3. Two Cartesian coordinate systems are defined with a space-fixed $oxyz$ coordinate system and a body-fixed $o'x'y'z'$ coordinate system. When the DPFB is located at its equilibrium stage, the two space coordinates fully coincide with each other. The total computational domain consists of the outer water surface S_{Fo} , the internal water surface S_{Fi} , the body surface S_B , the seabed surface S_D and the side surface S_C . Based on the assumption of non-viscous, incompressible and irrotational fluid, the water motion can be described by a velocity potential Φ which satisfies the Laplace governing equation and the following boundary conditions.

$$\frac{d(x, y, z)}{dt} = \frac{\partial \Phi}{\partial(x, y, z)} \quad \text{on SFo and SFi} \quad (12)$$

$$\frac{d\Phi}{dt} = \frac{1}{2} |\nabla \Phi|^2 - g\eta - \frac{P_a}{\rho_w} \quad \text{on SFo and SFi} \quad (13)$$

$$\frac{\partial \Phi}{\partial n} = (\vec{V} + \vec{\theta} \times \vec{r}') \cdot \vec{n} \quad \text{on SB} \quad (14)$$

$$\frac{\partial \Phi}{\partial n} = 0 \quad \text{on SC and SD} \quad (15)$$

where η denotes the water surface elevation. \vec{V} and $\vec{\theta}$ is the translational and rotational velocity vectors of the DPFB, respectively. \vec{r}' the coordinate vector in the body-fixed coordinate system. \vec{n} is the normal vector on the body surface pointing out the computational domain. P_a is the air pressure above water surface, i.e. $P_a = 0$ outside chamber and $P_a = p$ pneumatic pressure inside chamber. The pneumatic pressure in chamber is quadratic relationship with the air flow velocity $U_a(t)$ as follows

$$P_a = \frac{\rho_a}{2} \left(\frac{1}{\alpha C_c} - 1 \right)^2 |U_a(t)| U_a(t) \quad (16)$$

where ρ_a and $U_a(t)$ are the air density and the air flow velocity, respectively. C_c is the contraction coefficient obtained from the Chisholm expression (Fossa and Guglielmini, 2002).

$$C_c = \frac{1}{0.639(1 - \alpha)^{0.5} + 1} \quad (17)$$

The air flow velocity $U_a(t)$ in Eq. (16) can be calculated according to the change of the air volume in the OWC chamber

$$U_a(t) = \frac{V_{t+\Delta t} - V_t}{A_o \Delta t} \quad (18)$$

where $V_{t+\Delta t}$ and V_t denote the air volume at time $t+\Delta t$ and t , respectively, which are obtained by integrating the water surface across the chamber at each time step.

The initial condition at $t = 0$ in the numerical model is defined as the DPFB installed in the incident waves suddenly. Through Green's law, the Laplace equation in the computational domain can be transferred into a

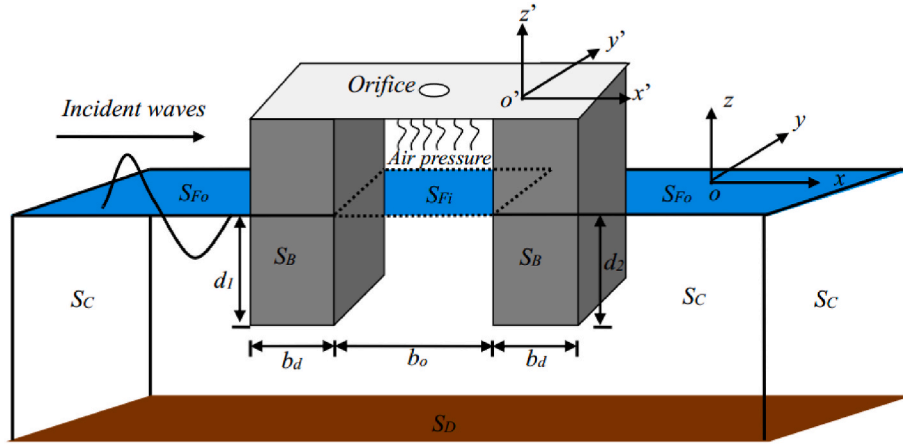


Fig. 3. Definition sketch of 3D waves interact with a WEC-type floating breakwater.

water integral equation over its closed surfaces which are divided into many higher-order elements i.e. eight node quadratic isoparametric elements. The potential and its normal derivative are interpolated by using the shape functions. Boundary conditions are used, and the unknowns are then obtained from the solution of the matrix equation. Once the solution of the above boundary problem is solved, the hydrodynamic loads on the body surface can be obtained as

$$F_i = -\rho_w \iint_{S_B} \left(\frac{\partial \Phi}{\partial t} + \frac{1}{2} |\nabla \Phi|^2 + gz \right) \cdot n_i dS \quad (19)$$

where F_i ($i = 1, 2$ or 3) denotes the hydrodynamic force along x , y or z direction and F_i ($i = 4, 5$ or 6) denotes the hydrodynamic moment about x , y or z direction.

Based on Newton's second law, the heave motion equation of the FB can be expressed as

$$m \ddot{\zeta} + b_{pto} \dot{\zeta} = F_3 \quad (20)$$

where m is the body mass. The nonlinear hydrodynamic load F_3 can be calculated by introducing the auxiliary function ψ , and thus Eq. (20) can be written as

$$(m + K) \ddot{\zeta} + b_{pto} \dot{\zeta} = Q_3 \quad (21)$$

where

$$K = \rho_w \iint_{S_B} \psi \cdot n_3 dS \quad (22)$$

$$Q_3 = -\rho_w \iint_{S_B + S_{Fo} + S_{Fi}} \left(\frac{1}{2} |\nabla \Phi|^2 + gz \right) \cdot \frac{\partial \psi}{\partial n} dS + \rho_w \int_{S_B} \nabla \psi \cdot \zeta \cdot n_3 \cdot \nabla \Phi dS \quad (23)$$

The elements on the boundary surfaces are generated based on the soft-ware Gambit at the initial time. After solving the motion of water and structure, the nodes of elements move both horizontally and vertically in the Lagrangian frame of the water surface condition. Hence, the discrete elements would cluster and scatter in the process of updating, and mesh rearrangement on water surface should be implemented. This paper adopts a spring analogy method proposed by Ma et al. (2010) to redistribute all nodes with keeping their connectivity. The new coordinates of node i can be expressed

$$\mathbf{X}_i^{t+\Delta t} = \mathbf{X}_i^t + \delta_i \quad (24)$$

where δ_i is the displacement vector of node I and can be solved by using Jacobi iterative form, i.e.

$$\delta_i = \frac{\sum_{j=1}^{N_i} K_{ij} \delta_j}{\sum_{j=1}^{N_i} K_{ij}} \quad (25)$$

where N_i denotes the total number of adjacent nodes; K_{ij} denotes the linear stiffness.

3.2. Comparison with experimental data

A three-dimensional (3D) numerical model is established to reproduce the experiments, and its dimensions including length, width and water depth are same with those of the physical flume. The width and draft of the OB-type SPFB are set as $b_s = 0.3$ m and $d_s = 0.15$ m, respectively. The geometrical parameters of the OWC-type DPFB are $b_d = 0.15$ m, $d_1 = d_2 = 0.15$ m and $b_o = 0.25$ m. The PTO damping coefficients for the OB and OWC devices are set as the opening ratio $\alpha = 0.769\%$ and the damping coefficient $b_{pto} = 150$ N/m. After conducting the mesh and time convergence (Cheng et al., 2022), the mesh size on the water surface is $\Delta x = \Delta y = \lambda/10$, where λ is the wavelength. On the body surface, the element length is set as $\lambda/15$ along the horizontal and vertical directions. The total time of 25 wave periods is selected with a uniform time step $dt = T/60$.

Fig. 4 shows the numerical and experimental comparison of the time series of the SPFB heave for $H_i = 0.10$ m and $T = 1.0$ s. The present

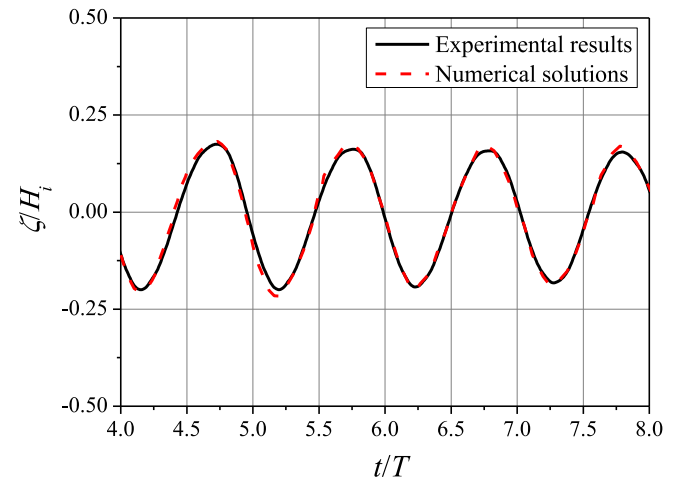


Fig. 4. Time series of the measured and predicted heave motion of the OB-type SPFB.

numerical results agree well with the experimental data with a small phase difference of around 2%, and a maximum amplitude difference of 7%. The slightly overestimation of the heave motion can be attributed to the in-viscous assumption. Additionally, the gap between the flume wall and the body would induce the transverse sloshing motion of water, affecting the measured accuracy. Furthermore, Fig. 5(a) and (b) display the time series of the wave elevation and the air pressure in the OWC chamber for the OWC-type DPFB, respectively. The distinct nonlinear phenomenon can be observed in the curves of the wave elevation and the air pressure, i.e. multiple peaks or valleys, steeper variation in wave trough and asymmetry of peaks and valleys. The higher-order components are clearly captured by the fully nonlinear numerical model.

The contributions from different order non-linear components, such as fundamental, second- and third-order, have been obtained by use of the fast Fourier transformation(FFT), and plotted against the dimensionless wave frequency ω/ω_0 (ω_0 is the incident wave frequency) in Fig. 6(a) and (b). The relative error between numerical and experimental results δ as expressed in Eq. (43) for each order decompositions are also indicated in these figures. It can be seen that the different-order contributions exist i.e. up to the fourth-order for wave elevation and the third-order for air pressure. The frequencies of n-order components correspond to n times wave frequency. The percentages of the total arising from the fundamental to fourth-order components for wave elevation are calculated as 77.31%, 7.73%, 13.53% and 1.43, and those for air pressure are 87.20%, 8.72%, 2.90% and 1.18%, respectively. Although the fundamental component is dominant to both wave elevation and air pressure, the contributions of the higher-order components can not be ignored, and are associated with nonlinear wave in Eq. (13) and quadratic air pressure Eq. (16).

$$\delta = \frac{|S_{\eta/P}^N - S_{\eta/P}^E|}{S_{\eta/P}^E} \quad (43)$$

where the superscripts *N* and *E* denote the numerical and experimental spectral values, respectively.

4. Results and discussion

In this section, the dependence of the OB-type SPFB and the OWC-type DPFB on the designed parameters is firstly investigated in detail. Then, the hydrodynamic comparison of the two type FBs is presented in terms of the wave transmission coefficient and wave energy conversion efficiency. Furthermore, the effect of wave nonlinearity i.e. incident wave height is examined. All results are obtained from experimental tests. The main objective is to provide the improved knowledge to design a hybrid WEC-FB system with favorable performance.

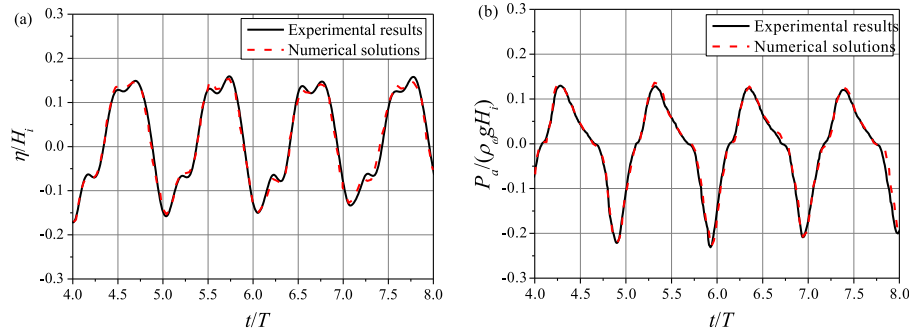


Fig. 5. Time series of the measured and predicted (a) wave elevation and (b) air pressure in the chamber of the OWC-type DPFB.

4.1. Hydrodynamic performance of the OB-type SPFB

4.1.1. Effect of draft

Experiments were conducted with three different drafts ($d_s = 0.1$ m, 0.15 m, and 0.2 m) for the OB-type FB with PTO damping $b_{pto} = 150$ N s/m. The incoming wave height is kept to $H_i = 0.1$ m, and other variables has been described in Section 2.1. Fig. 7(a) and (b) display the variation of the reflection coefficient and the transmission coefficient with the dimensionless wave period $T(g/H_i)^{1/2}$, respectively. It can be seen from Fig. 7(a) that the reflection coefficient is basically unchanged by the body draft with exception of the region $13 < T(g/H_i)^{1/2} < 15$ in which the reflection coefficient increases with d . This is due the fact that the short wave energy is mainly concentrated near the water surface with the range of a wave height, and decays rapidly along water depth. In this particular case, three tested drafts are larger than incident wave height, and have weak effects on the reflection coefficient. On the contrary, for the long wave region $13 < T(g/H_i)^{1/2} < 15$, the motion velocity of water particles decays more slowly along water depth. Consequently, the effective seaward area of the FB increases with draft, which leads to a larger reflection coefficient. As shown in Fig. 7(b), the transmission coefficient increases with increasing the body draft for the whole range of wave periods. This means that the attenuation capacity of the SPFB is mainly a function of the body draft, which is consistent with the observation by Zhang et al. (2021) (focused on a typical SPFB device).

Fig. 8(a) and (b) show the heave RAO and the energy conversion efficiency of the OB-type SPFB for different body drafts. It can be seen from Fig. 8(a) that the heave motion of the SPFB decreases with increasing body draft in short-period waves but is insensitive to the draft in long-period waves. A similar trend for the conversion efficiency curves can be also observed in Fig. 8(b). This is closely related to the wave energy distribution along water depth. A shallower draft leads to more effectively interaction with short-period waves to a higher absorption of wave energy. Additionally, the maximum energy conversion efficiency is shifted from left to right side that has larger values of $T(g/H_i)^{1/2}$. This shift can be associated with the formula of the resonant period of the SPFB as follows (Zhang et al., 2021a,b)

$$T_s = \sqrt{\frac{4\pi^2(\rho_w g L b_s d_s + a_z)}{\rho_w g L b_s}} \quad (44)$$

where T_s is the resonant periods for the OB; a_z is the added mass. It is clear from Eq. (44) that the resonant period of the SPFB increases with increasing body draft.

4.1.2. Effect of PTO dampings

In this sub-section, three different PTO dampings (i.e. $b_{pto} = 40$ N s/m, 150 N s/m and 300 N s/m), are selected to illustrate the effect of the PTO system for the OB-type SPFB. The draft of the SPFB is fixed as $d_s = 0.15$ m and other parameters are kept the same with Figs. 7 and 8. Fig. 9 (a) and (b) give distribution of the reflection and transmission coefficients with wave period for different PTO dampings. It can be seen

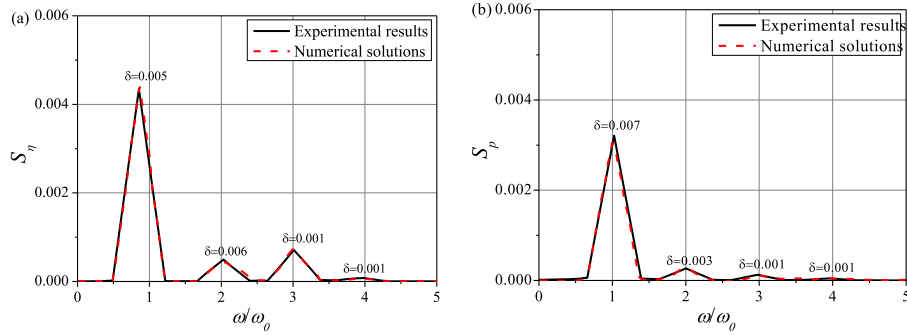


Fig. 6. Spectra analysis of (a) wave elevation and (b) air pressure in the chamber of the OWC-type DPPFB.

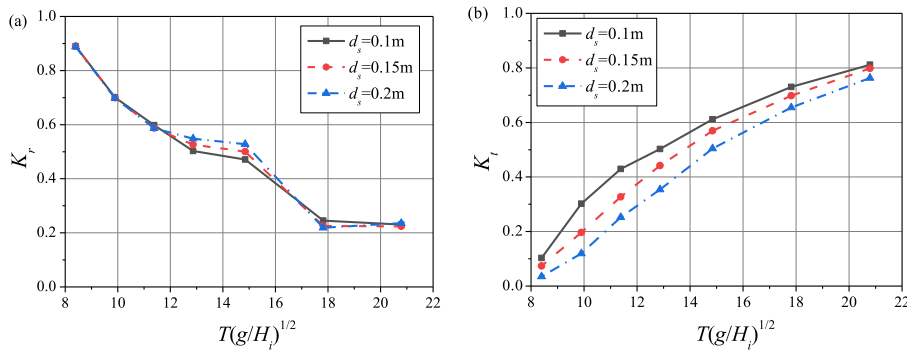


Fig. 7. Variations of (a) the reflection coefficient K_r and (b) the transmission coefficient K_t with dimensionless wave period $T(g/H)^{1/2}$ for three different drafts of the OB-type SPFB.

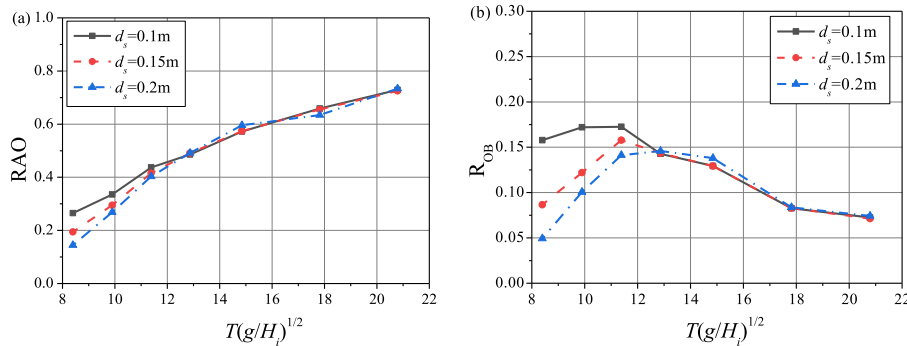


Fig. 8. Variations of (a) the heave RAO and (b) the energy conversion efficiency R_{OB} with dimensionless wave period $T(g/H)^{1/2}$ for three different drafts of the OB-type SPFB.

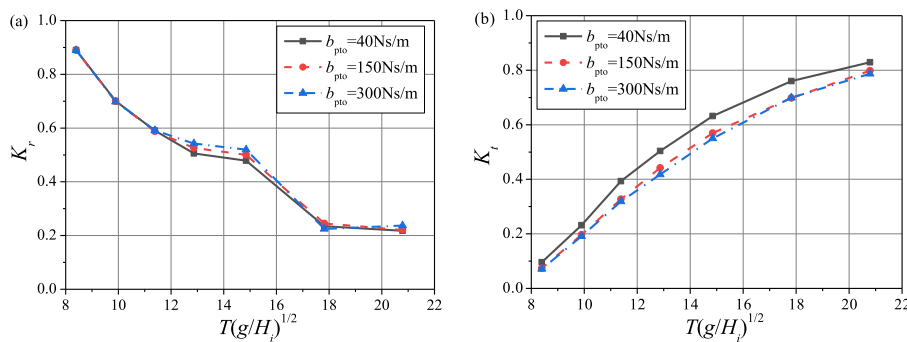


Fig. 9. Variations of (a) the reflection coefficient K_r and (b) the transmission coefficient K_t with dimensionless wave period $T(g/H)^{1/2}$ for three different PTO damping coefficients of the OB-type SPFB.

from Fig. 9(a) that the reflection coefficient increases with increasing PTO damping in long-period waves ($T(g/H_i)^{1/2} > 12$). This can be explained by the fact that the motion response of the SPFB increases with decreasing PTO damping, which causes more wave energy dissipation including the viscous energy losses and flow separation at the bottom edges. Fig. 9(b) reveals that the transmission coefficient decreases apparently with increasing b_{pto} from 40 N s/m to 150 N s/m, and then almost remains identical after that. This is not surprising because a larger PTO damping leads to a higher wave energy absorption at the initial stage of increasing PTO damping. When the PTO damping increases to the optimal damping, the wave energy extraction reaches the maximum. With further increasing PTO damping, the attenuation performance of the SPFB is close to that of the fixed breakwater. The optimal damping b_{opt} based on linear wave theory can be obtained as follows (Zhang et al., 2021a,b)

$$b_{opt} = \sqrt{\frac{(m_s + a_z)\omega^2 - (\rho_w g L b_s)^2}{\omega^2}} + b_z \quad (45)$$

where b_z is the radiation damping coefficient of the SPFB.

The distribution of the heave RAO and the energy conversion efficiency for different PTO dampings of the OB-type SPFB is given in Fig. 10(a) and (b), respectively. As can be intuitively expected, the motion response of the SPFB is reduced with increasing as shown in Fig. 10(a). In Fig. 10(b), the SPFB becomes more advantageous for extracting wave energy with increasing b_{pto} from 40 N s/m to 150 N s/m. However, with further increasing b_{pto} from 150 N s/m to 300 N s/m, the energy conversion efficiency decreases in the short-period wave region of $T(g/H_i)^{1/2} < 16$ and increases in the long-period wave region of $T(g/H_i)^{1/2} > 16$. This phenomenon is due to that the optimal PTO damping increases with increasing wave period. According to Eq. (45), the optimal PTO damping is closer to 150 N s/m than 300 N s/m for $T(g/H_i)^{1/2} < 16$, and vice versa for $T(g/H_i)^{1/2} > 16$. The maximum energy conversion efficiencies corresponding to the resonant period $T(g/H_i)^{1/2} = 11.38$ are $R_{OB} = 0.14, 0.16$ and 0.12 for $b_{pto} = 40$ N s/m, 150 N s/m and 300 N s/m, respectively. This demonstrates that the wave energy is the highest when the wave period is around the resonant period and the PTO damping is simultaneously the optimal damping i.e. radiation damping.

4.2. Hydrodynamic performance of the OWC-type DPFB

4.2.1. Effect of draft

The draft of the OWC-type DPFB includes the drafts of the front and back pontoons denoted respectively by d_1 and d_2 , as verified in Fig. 3. Fig. 11 shows the variation of the reflection coefficient, the transmission coefficient, the wave coefficient in the chamber and the energy conversion efficiency of the DPFB with wave period for different pontoon drafts. From Fig. 11(a), it can be concluded that the reflection coefficient is unaffected by the pontoon draft in short-period waves and increases

with increasing pontoon draft in long-period waves because of the strong transmission ability of long-period waves. Part of wave energy of long-period waves that enters into the chamber can be further reflected by the back pontoon. In Fig. 11(b), the variation of the transmission coefficient against pontoon draft for the OWC-type DPFB is similar to that of the OB-type SPFB as shown in Fig. 7(b). It is worth mentioning from Fig. 11(c) that the wave elevation in the OWC chamber decreases with increasing the pontoon draft in short-period waves but is almost the same in long-period waves. This is because the short-period waves can be easily reflected by the front pontoon and the waves weakly transmit into the OWC chamber. Fig. 11(d) indicated that both the maximum energy conversion efficiency and effective frequency bandwidth decreases with increasing the pontoon draft, with the maximum $R_{OWC} = 0.18, 0.15$ and 0.12 respectively. According to the following approximated formula for the water motion in a moonpool, the resonant periods of the water column in the OWC chamber are $T_d(g/H_i)^{1/2} = 7.72, 8.91$ and 9.89 for $d_1 = d_2 = 0.10$ m, $d_1 = d_2 = 0.15$ m and $d_1 = d_2 = 0.20$ m, respectively, but the maximum energy conversion efficiency corresponds to the same period $T_d(g/H_i)^{1/2} = 11.38$ for all drafts. This is due to that the coefficient 0.41 in Eq. (44) is empirical and is determined by the fitting technique. Hence, the accurate resonant period for the OWC with different configurations should be done with rigorous tests. The resonant period of the water in the OWC chamber is independent on the pontoon draft (Veer and Thorlen, 2008).

$$T_d = -\sqrt{\frac{4\pi^2(d_1 + 0.41\sqrt{A_w})}{g}} \quad (44a)$$

To further analyze the effect of the front-pontoon draft, three drafts of the front pontoon (i.e. $d_1 = 0.10$ m, 0.15 m and 0.20 m) are considered with the draft of the back pontoon kept the same (i.e. $d_2 = 0.20$ m). The distribution of the reflection coefficient, the transmission coefficient, the wave coefficient in the chamber and the energy conversion efficiency with wave period is shown in Fig. 12(a)-(d), respectively. It is remarkable from Fig. 12(a) that the reflection coefficient is insensitive to d_1 in short-period waves and increases with d_1 in long-period waves due to the amplification of the effective seaward area in the direction normal to the wave propagation. As shown in Fig. 12(b), the transmission coefficient decreases with increasing the draft of the front pontoon, especially near the resonant region of $10 < T_d(g/H_i)^{1/2} < 14$. It can be seen from Fig. 12(c) that larger wave elevations in the chamber are measured for smaller drafts of the front pontoon. This is because that waves can be more easily reflected by the front pontoon with larger drafts. It should be noted that the draft of the front pontoon has an obvious influence on the energy conversion efficiency, and a shallower front-pontoon draft leads to a higher conversion efficiency in the OWC chamber, with the maximum $R_{OWC} = 0.25, 0.17$ and 0.12 respectively. The effective frequency bandwidth is extended and can be seen to shift to the short-period wave region.

Then, what will happen if the front-pontoon draft is kept the same,

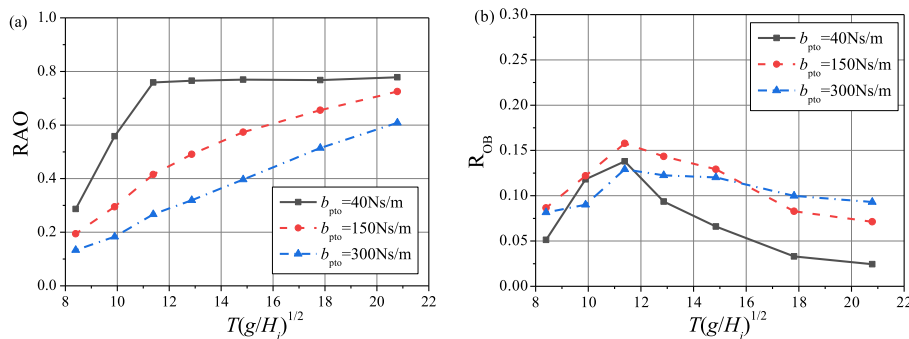


Fig. 10. Variations of (a) the heave RAO and (b) the energy conversion efficiency R_{OB} with dimensionless wave period $T(g/H_i)^{1/2}$ for three PTO damping coefficients of the OB-type SPFB.

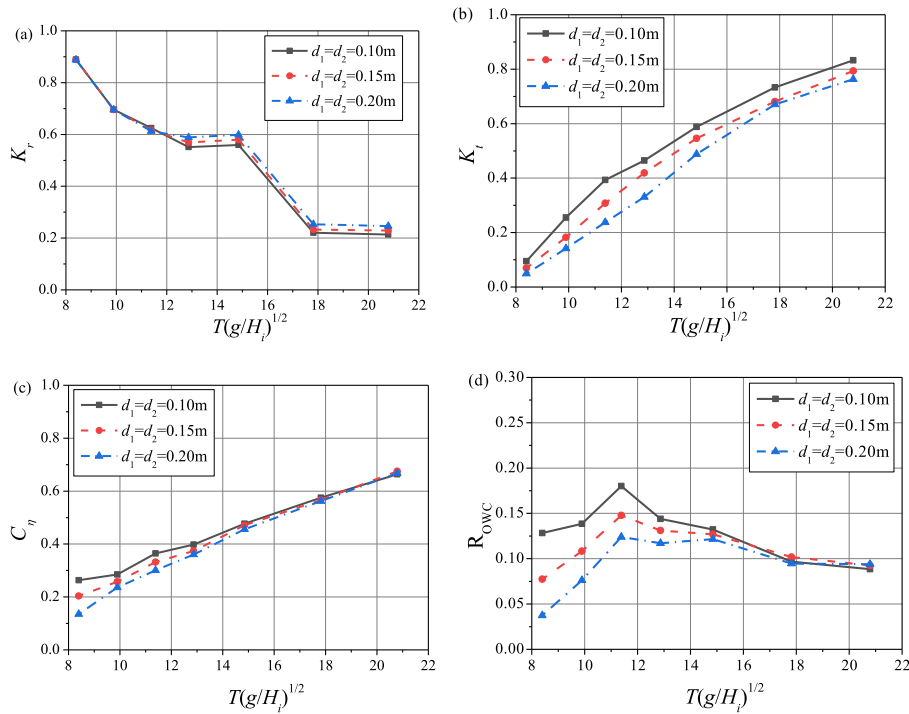


Fig. 11. Variations of (a) the reflection coefficient K_r , (b) the transmission coefficient K_t , (c) the wave coefficient C_η in the chamber and (d) the conversion efficiency R_{OWC} with dimensionless wave period $T(g/H_1)^{1/2}$ for three different pontoon drafts of the OWC-type DPFB.

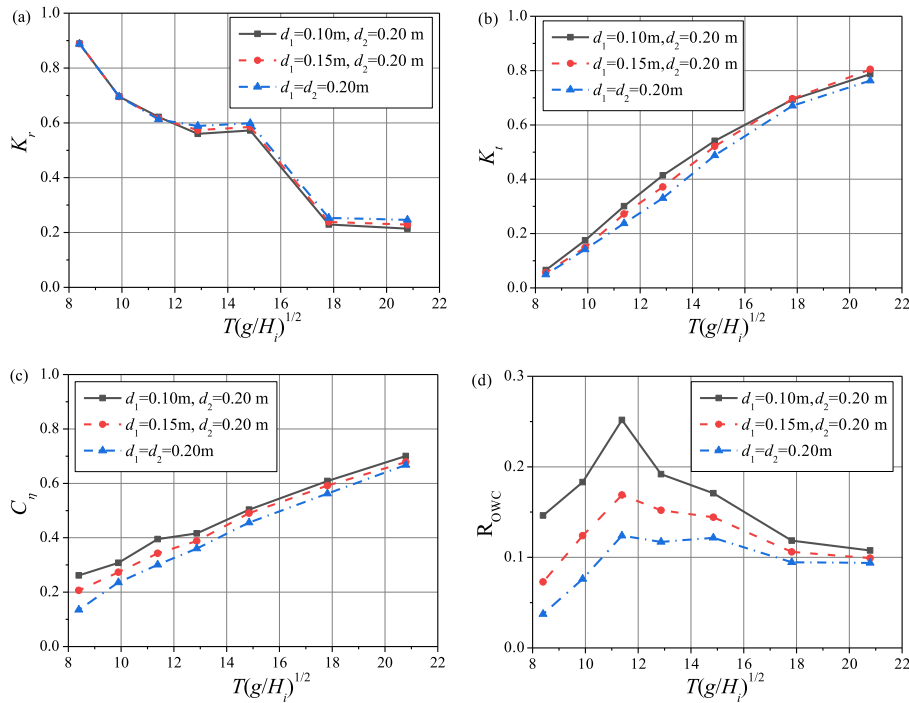


Fig. 12. Effects of the front-pontoon draft on (a) the reflection coefficient K_r , (b) the transmission coefficient K_t , (c) the wave coefficient C_η in the chamber and (d) the conversion efficiency R_{OWC} of the OWC-type DPFB.

while the back-pontoon draft changes? To answer this question, three back-pontoon drafts (i.e. $d_2 = 0.10\text{ m}$, 0.15 m and 0.20 m) are selected while keeping the same front-pontoon draft $d_1 = 0.10\text{ m}$. Fig. 13 presents the variation of the reflection coefficient, the transmission coefficient, the wave coefficient in the chamber and the energy conversion efficiency for different back-pontoon drafts. From Fig. 13(a), it can be seen

that the back-pontoon draft has a weaker influence on the reflection coefficient than that of the front-pontoon. The transmission coefficient decreases monotonically with increasing the back-pontoon draft, as shown in Fig. 13(b). This is reasonable since the back-pontoon has a larger draft which leads to much stronger water motion in chamber as shown in Fig. 13(c) and thus more wave energy is dissipated. The effect

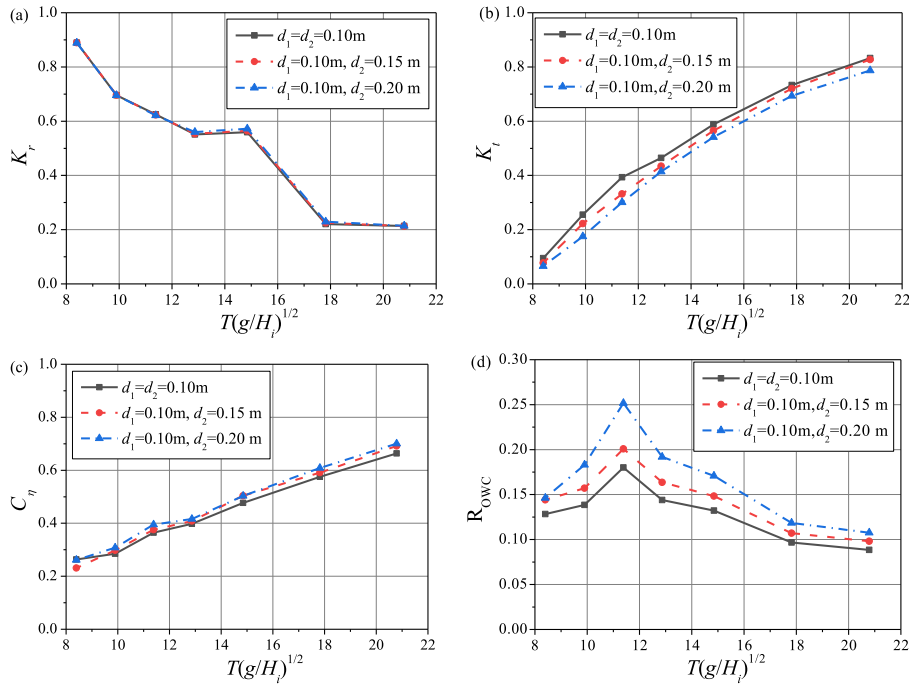


Fig. 13. Effects of the back-pontoon draft on (a) the reflection coefficient K_r , (b) the transmission coefficient K_t , (c) the wave coefficient C_η in the chamber and (d) the conversion efficiency R_{OWC} of the OWC-type DPFB.

of the back-pontoon draft on the water motion is in contrast to that of the front-pontoon draft. Fig. 13(d) reveals that the wave reflection by the back-pontoon can enhance the energy extraction performance of the OWC device. The maximum conversion efficiency of the OWC-type DPFB is strongly influenced by the back-pontoon draft with $R_{OWC} = 0.18$ ($d_2 = 0.10$ m), 0.20 ($d_2 = 0.15$ m) and 0.25 ($d_2 = 0.20$ m). A similar conclusion was ever by Ning et al. (2017) in their experimental investigation on an offshore fixed cylindrical dual-chamber OWC. It can be

concluded that for practical engineering applications such as wave energy exploitation or marine protection, the OWC-type DPFB with a larger back-pontoon draft and a smaller front-pontoon draft would be preferred, because not only both higher wave energy extraction can be realized, and better wave attenuation capacity is achieved.

4.2.2. Effect of chamber width

The effect of the chamber width i.e. the gap distance between two

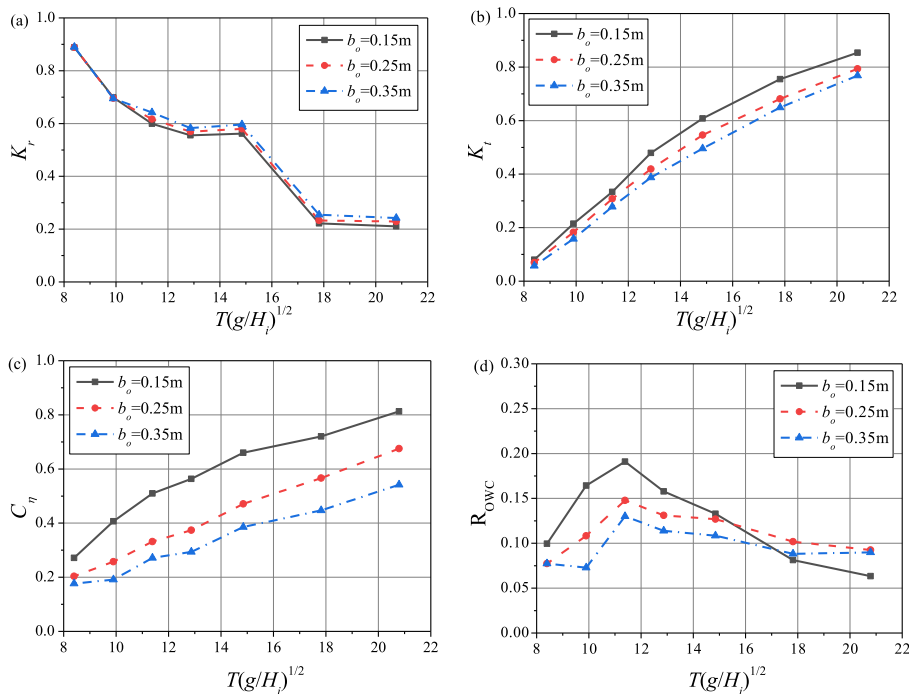


Fig. 14. Variations of (a) the reflection coefficient K_r , (b) the transmission coefficient K_t , (c) the wave coefficient C_η in the chamber and (d) the conversion efficiency R_{OWC} with dimensionless wave period $T(g/H_l)^{1/2}$ for three different chamber widths of the OWC-type DPFB.

pontoons is discerned in this sub-section, and three sets of chamber widths (i.e. $b_o = 0.15$ m, 0.25 m and 0.35 m) are selected. It is noted that the widths of the two pontoon are kept the same in this paper. The identical drafts of the front-pontoon and the back-pontoon are set as $d_1 = d_2 = 0.15$ m. Fig. 14(a)-(d) shows the variation of the reflection coefficient, the transmission coefficient, the wave coefficient in the chamber and the energy conversion efficiency with wave period. It can be found from Fig. 14(a) that the reflection coefficient slightly increases with increasing chamber width in long-period waves. This is attributed to the reason that the water volume in the chamber increases with increasing the chamber width. Hence, more water motion can be induced by the waves transmitting into the chamber. This energy exchange between outer waves and internal water causes lower transmission coefficient, as shown in Fig. 14(b). In Fig. 14(c), the wave elevation in the chamber decreases with increasing chamber width, leading to smaller gap resonance effect as the internal water oscillates up and down. In this scenario, the fatigue damage to the inner body surfaces between the two pontoons can be avoided. It is emphasized from Fig. 14 (d) that the energy conversion efficiency decreases with increasing chamber width in short-period waves. This is attributed to that a smaller chamber width leads to a smaller air volume in the chamber, which induces more violent change of the internal water motion and the pneumatic pressure. In long-period waves, the conversion efficiency decreases more slowly for larger chamber width compared with that for smaller chamber width. This is because long-period wave energy with high transmission ability can be fully absorbed by the large chamber.

4.2.3. Effect of opening ratio

In order to obtain the optimal PTO damping for the OWC-type DPFB, three opening ratios ($\alpha = 0.398\%$, 0.769% and 1.272%) are considered, which correspond to the diameters of the circular orifices $D = 0.025$ m, 0.035 m and 0.045 m, respectively. The OWC chamber width is $b_o = 0.25$ m and other parameters are kept the same with those in Fig. 14. Fig. 15(a)-(d) illustrate the effects of the opening ratio on the reflection coefficient, the transmission coefficient, the wave coefficient in the chamber and the energy conversion efficiency, respectively. From

Fig. 15(a), it can be seen that the reflection coefficient slightly decreases with increasing the opening ratio. This is because the total reflection includes the reflections from the front pontoon, the back pontoon and below the water column in the chamber. The PTO damping in the chamber decreases with increasing the opening ratio, resulting in a stronger water motion in the chamber which is in accordance with the results as shown in Fig. 15(c). Consequently, the reflection from the internal water column is reduced with the opening ratio. However, the transmission coefficient is insensitive to the opening ratio, which is because of the energy exchange between the incoming waves, reflected waves and the internal water motion. As shown in Fig. 15(d), the maximum energy conversion efficiency increases with increasing the opening ratio, even though the effective frequency bandwidth is unchanged. The opening ratio for maximum efficiency is larger than $\alpha = 1.272\%$. It is interesting that the energy conversion efficiency for $\alpha = 0.398\%$ increases when wave period increases from $T_d(g/H_i)^{1/2} = 18$ to 21 . This is due to the fact that the long-period waves with a higher energy flux intensity enter into the chamber more easily, and thus a smaller orifice (larger PTO damping) can induce larger air pressure in the chamber, enhancing the wave energy extraction of the OWC device.

4.3. Comparison of the OB-type SPFB and the OWC-type DPFB

4.3.1. Reflection and transmission coefficients

In this sub-section, the hydrodynamic coefficients i.e. the reflection and transmission coefficients of the OB-type SPFB is compared with those of the OWC-type DPFB. The pontoon width of the SPFB is equal to the overall pontoon width of the DPFB, i.e. $b_s = 2b_d = 0.3$ m. Their displacements i.e. structural masses are kept same, i.e. $V = 0.035$ m³. Therefore, three combination of pontoon drafts are considered, $d_s = 0.15$ m for SPFB, $d_1 = d_2 = 0.15$ m for DPFB and $d_1 = 0.10$ m and $d_2 = 0.20$ m for DPFB. Fig. 16(a) and (b) display the comparisons of the reflection and transmission coefficients of the DPFB with different drafts and the SPFB. From Fig. 16(a), it can be seen that in the period region of $10 < T_d(g/H_i)^{1/2} < 14$, due to the amplification of the effective seaward area, the reflection coefficient of the OB-type SPFB is smaller than that of

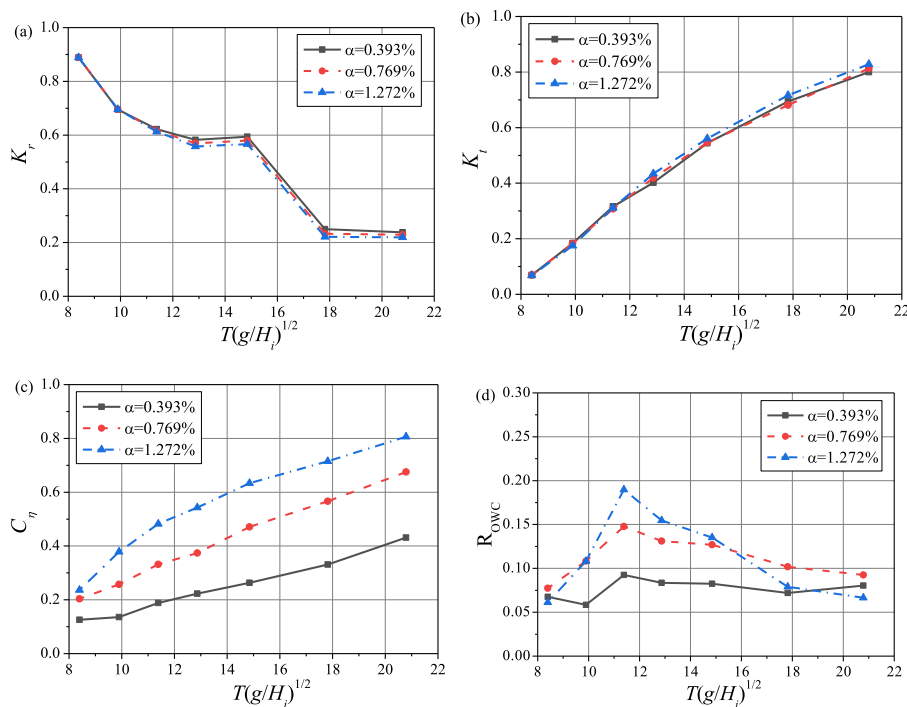


Fig. 15. Variations of (a) the reflection coefficient K_r , (b) the transmission coefficient K_t , (c) the wave coefficient C_η in the chamber and (d) the conversion efficiency R_{OWC} with dimensionless wave period $T(g/H_i)^{1/2}$ for three different opening ratios of the OWC-type DPFB.

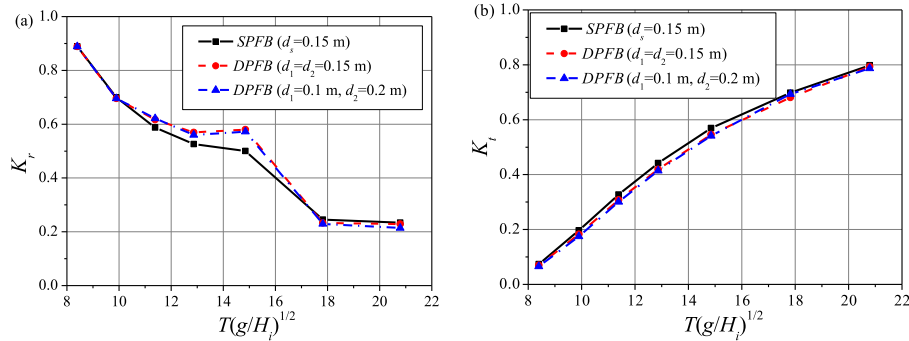


Fig. 16. Comparison of (a) the reflection coefficient K_r and (b) the transmission coefficient K_t of the OB-type SPFB and the OWC-type DPFB for different combinations of pontoon draft.

the OWC-type DPFB. In contrast, in long-period wave region, part of wave energy is transmitted into the chamber and is absorbed by the OWC device, leading to the smaller reflection of the DPFB compared to that of the SPFB. As shown in Fig. 16(b), the transmission coefficient of the DPFB with different drafts is smaller than that of the SPFB for the whole range of wave periods. It is noted that the transmission coefficient is used as a basis for the wave attenuation ability of the FB. This finding suggests that the wave attenuation of the pontoon-type FB can be enhanced by integrating OWC devices into the gap between pontoons.

Next, the comparisons of the reflection and transmission coefficients of the OWC-type DPFB with different chamber widths (i.e. gap distances between two pontoons) and the OB-type SPFB are shown in Fig. 17(a) and (b). The drafts of all pontoons are set as 0.15 m and other parameters have been given in Fig. 15. It can be seen from Fig. 17(a) that the reflection coefficient of the DPFB can be diminished by the small gap due to the more wave energy dissipation generated by the gap resonance, but is still larger than that of the SPFB in moderate-length wave region. Combing Figs. 17(b) and 16(b), from the direct comparison of the transmission coefficient of the DPFB with different chamber widths and the SPFB, it can be found that when the chamber width is smaller than a critical value i.e. 0.25 m in this paper, the gap design for the DPFB become disadvantageous in terms of the wave attenuation performance. This enlighten us that the gap distance does not always reduce the transmission coefficient, and the effectiveness of the single pontoon width and the chamber width should be weighed based on the energy transform. The optimal ratio of the chamber width of the total pontoon width is larger than 0.83, which leads to a larger wave energy absorbed by the water in the OWC than that absorbed by the OB motion.

4.3.2. Energy conversion efficiency

The comparisons of the energy conversion efficiency for the OWC-type DPFB with different designed parameters and the OB-type SPFB are plotted in Fig. 18(a)-(c). Fig. 18(a) shows that the energy extraction

of the OWC device with a shallower front-pontoon draft and a deeper back-pontoon draft is significantly higher than that of the OB device when the displacements of the two devices are kept the same. This is because a larger difference between the drafts of the back and front pontoons means a longer, heavier water column converged in the chamber as well as more fully interaction between the water outside and inside the chamber when the draft of the front-pontoon draft is smaller than that of the back-pontoon draft. When the drafts of all pontoons are the same and the ratio of the chamber width and the total pontoon width is larger than 0.83, the conversion efficiency of the OWC is lower than that of the OB in short-period waves, and the opposite is true in long-period waves, as shown in Fig. 18(b). Considering the optimal PTO damping coefficients, the maximum energy conversion of the OWC device is enhanced compared to the OB device, by up to 1.26 times, with almost identical effective frequency bandwidth, as indicated in Fig. 18 (c).

4.4. Wave nonlinear factors

According to the linear wave theory, both the wave attenuation and the energy conversion should be independent on the incident wave height H_i . However, some higher-harmonic wave components are generated by the interaction of waves with large amplitude and floating bodies, even to be comparable to the fundamental waves due to strong instantaneous motion of the intersection line between water surface and body surfaces. Therefore, three incident wave heights $H_i = 0.05$ m, 0.10 m and 0.15 m are considered and other parameters are the same with those in Section 2.1. In order to compare the results among different wave heights, the dimensionless wave period in Figs. 19–21 was defined as $T(g/h)^{1/2}$.

4.4.1. Reflection and transmission coefficients

Fig. 19(a) and (b) shows the effect of the incident wave height on the

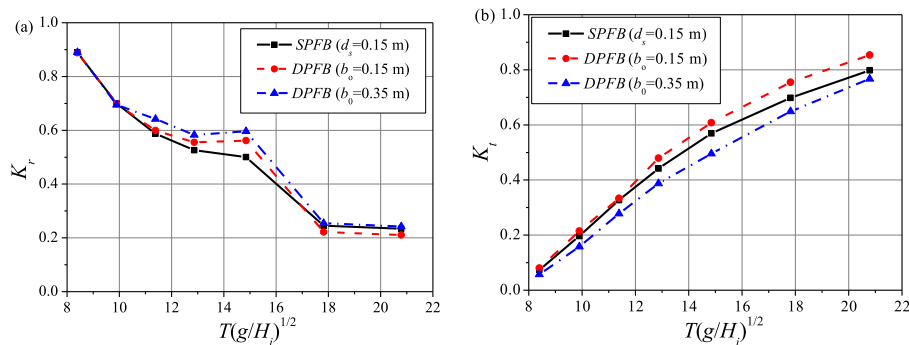


Fig. 17. Comparison of (a) the reflection coefficient K_r and (b) the transmission coefficient K_t of the OB-type SPFB and the OWC-type DPFB for different chamber widths.

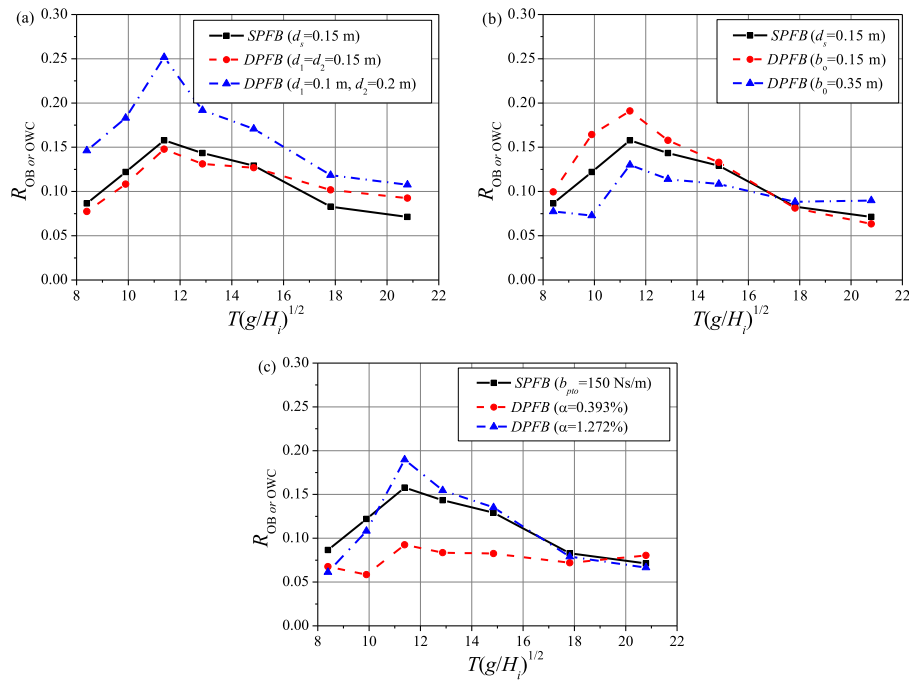


Fig. 18. Comparison of the energy conversion efficiency of the OB-type SPFB and the OWC-type DPFB for (a) different pontoon drafts, (b) different chamber widths and (c) different PTO damping coefficients.

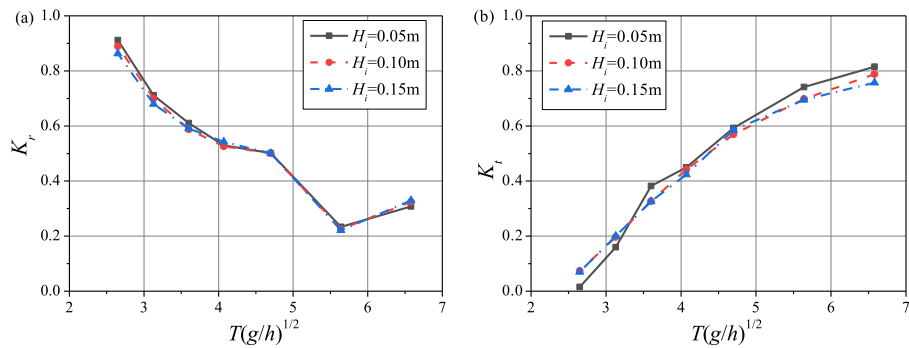


Fig. 19. Effects of incident wave height on (a) the reflection coefficient K_r and (b) the transmission coefficient K_t of the OB-type SPFB.

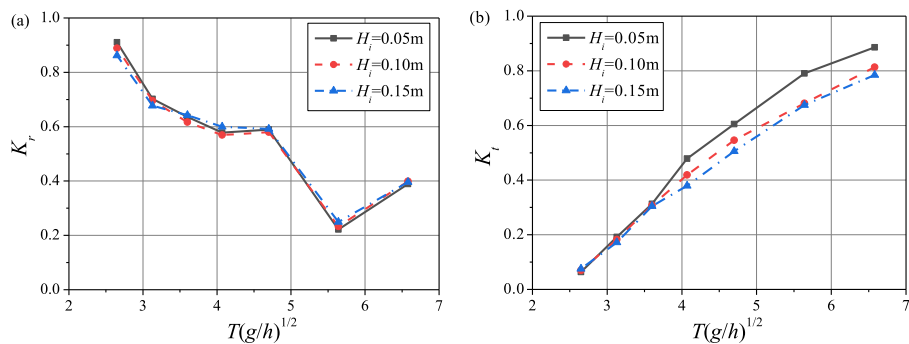


Fig. 20. Effects of incident wave height on (a) the reflection coefficient K_r and (b) the transmission coefficient K_t of the OWC-type DPFB.

reflection and transmission coefficients of the OB-type SPFB, respectively. It can be observed from Fig. 19(a) that the reflection coefficient in short-period waves moves slightly toward smaller values with increasing wave heights. This is because short-period waves with large amplitude are focused on the weather side of the OB, leading to more wave

breaking by the OB surface. As shown in Fig. 19(b), the wave nonlinearity has weak influence on the transmission coefficient, demonstrating that the model design for a particular range of periods and small wave height should also be adequate in the case of extreme wave conditions.

The reflection and transmission coefficients for the OWC-type DPFB

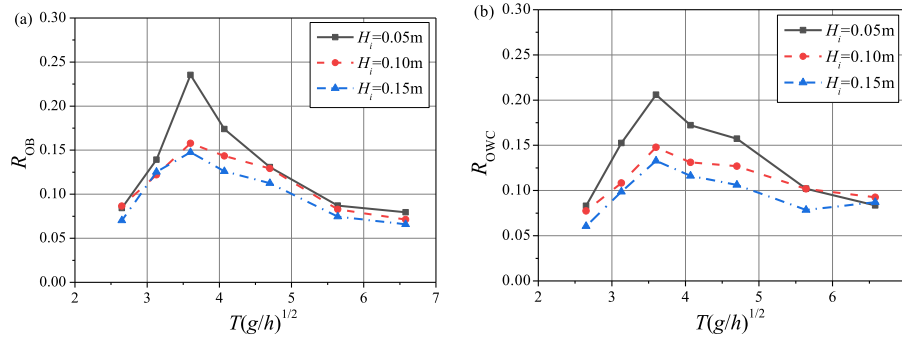


Fig. 21. Effects of incident wave height on (a) the conversion efficiency R_{OB} of the OB-type SPFB and (b) the conversion efficiency R_{OWC} of the OB-type SPFB.

are displayed in Fig. 20(a) and (b), respectively. The variation of the reflection coefficient in Fig. 20(a) is similar with that for the OB-type SPFB, and is insensitive to the wave height. However, the transmission coefficient apparently decreases with increasing wave height, especially in long-period waves. This is due to the fact that long-period waves with large amplitude enters into the OWC chamber to induce more violent water motion in the chamber. Some higher-order scattering waves including the bounded and free wave components are generated in the chamber and are easily re-reflected in the gap between pontoons. When the reflections from two pontoons meet in phase, the interference is constructive, leading to more wave energy dissipation. Additionally, the higher-order waves strength the variation of the air pressure in the chamber, which in turn accelerate the generation of higher-order waves.

Above findings enlighten us that the wave attenuation capacity of the OB-type SPFB can be accurately predicted by linear wave theory i.e. first-order potential flow theory, but that of the OWC-type SPFB should be simulated based on fully nonlinear theory due to the strong interaction among water, air and FB.

4.4.2. Energy conversion efficiency

Fig. 21(a) and (b) plot the effect of the wave height on the energy conversion efficiency of the OB-type SPFB and the OWC-type DPFB, respectively. The conversion efficiency of the OB-type SPFB in Fig. 21(a) decreases significantly with increasing wave height near the resonant period of the SPFB. This appears to be induced by the wave nonlinearity for $H_i > 0.05$ m, in which the stronger energy loss occurs i.e. the vortex in the seaward of the FB, the lee-wake vortices behind the body, the turbulence and the wave breaking. As presented in Fig. 21(b), the reduction of the conversion efficiency of the OWC-type DPFB with wave height covers the whole range of wave periods. This further means that the hydrodynamic performance of the OWC-type FB is strongly contingent on the degree of wave nonlinearity. To achieve higher energy conversion efficiency in a broader frequency bandwidth, the environmental conditions with small-amplitude waves are more appropriate.

5. Conclusions

Two WEC-type floating breakwater hybrid systems are considered in this study. One is single-pontoon floating breakwater (SPFB) as an OB device with heave motion only, and the other is dual-pontoon floating breakwater (DPFB) in which an OWC device is embedded in the gap between two pontoons. The principle is that the displacements and the total pontoon widths are kept the same for the two hybrid systems. A series of physical experiments were conducted to focus on the function of the wave attenuation and wave energy extraction simultaneously. The PTO systems for the two devices are modeled by an air aerodynamic damper installed between the fixed frame and the OB and a circular orifice located on the top of the OWC, respectively. Based on the fully nonlinear potential theory and the higher-order element method, a time-domain numerical model was developed to cross-check the experimental

data. The present numerical model was developed without the convergent restriction of small wave steepness; hence both fundamental and higher-order wave components can be considered to examine wave nonlinearity. The influence of the wave parameters, geometrical dimensions, gap distances between pontoons and PTO damping coefficients was experimentally investigated. Additionally, the hydrodynamic performance of the OB-type SPFB and the OWC-type DPFB are compared with each other. The following conclusions can be drawn.

The draft of the OB-type SPFB has strong influences on the wave attenuation capacity for most of wave periods examined as well as the wave energy extraction for short-wave periods less than the resonant period. As the PTO damping increases to the optimal damping near the resonant period in which the maximum conversion efficiency occurs, the transmission coefficient reaches its minimum and then remains about the same after that. For the OWC-type DPFB system, the purpose of the optimized design is to converge more wave energy in the gap between pontoons. Thus, a non-uniform pontoon draft can enhance energy conversion efficiency of the DPFB dramatically, but has no contribution to the wave transmission when the displacement is fixed. The influence of the chamber width on the wave attenuation is contrary to that on the maximum energy extraction. The wave attenuation is insensitive to the opening ratio but the maximum conversion efficiency is enhanced with an opening ratio being larger than 1.0%.

Comparisons of the OB-type SPFB and the OWC-type DPFB showed that the hydrodynamic performance for the DPFB with a small front-pontoon draft and a large back-pontoon draft is better than that for the SPFB with the same pontoon width and displacement. Under the premise of the same pontoon draft, when the ratio of the chamber width and the total pontoon width is larger than 0.83, the wave attenuation capacity of the DPFB design is higher than that of the SPFB, vice versa for the maximum energy conversion. Although the maximum conversion efficiency of the OB and OWC devices can be enhanced by the optimal PTO damping, the effective frequency bandwidth is not appreciably broadened.

In cases of stronger wave nonlinearity, the transmission coefficient is basically unchanged for the OB-type SPFB and is reduced for the OWC-type SPFB. The conversion efficiencies of the OB and OWC devices are diminished by wave nonlinearity. That is to say, the influence of the extreme wave conditions on the hydrodynamic performance of the OWC-type DPFB is more complicated compared to the OB-type SPFB.

The fully nonlinear factors including the large deformation of water surface and the instantaneous motion of floating bodies are considered in the developed numerical model. The corresponding experiments are conducted to further include the viscous effect, the vortices and the air compressibility. The findings of this study are of importance and helps to enhance the design of operational performance of such SPFB and DPFB devices. In the further work, we will examine the configuration of the array combining OBs and OWCs in multi-directional waves which are more realistic wave conditions.

CRediT authorship contribution statement

Yong Cheng: Methodology, Software, Data curation, Writing – original draft, Supervision. Lei Fu: Validation, Formal analysis, Writing – original draft, Investigation. Saishuai Dai: Formal analysis, Data curation, Writing – review & editing, Supervision. Maurizio Collu: Writing – review & editing, Supervision. Chunyan Ji: Writing – review & editing, administration. Zhiming Yuan: Writing – review & editing. Atilla Incecik: Supervision.

Declaration of competing interest

The authors declare that they have no known competing financial interests or personal relationships that could have appeared to influence the work reported in this paper.

Acknowledgment

The authors are grateful to the National Natural Science Foundation of China (Grant No. 52111530137, 52025112), the State Key Laboratory of Ocean Engineering, China (Shanghai Jiao Tong University) (Grant No. 1905) and the Newton Advanced Fellowships (Grant No. NAF\R1\180304) by the Royal Society for supporting this work.

References

- Brendmo, A., Falnes, J., Lillebekken, P.M., 1996. Linear modelling of oscillating water columns including viscous loss. *Appl. Ocean Res.* 18, 65–75.
- Cebada-Relea, A.J., López, M., Aenlle, M., 2022. Time-domain numerical modelling of the connector forces in a modular pontoon floating breakwater under regular and irregular oblique waves. *Ocean Eng.* 243, 110263.
- Chang, K.H., Tsaur, D.H., Huang, L.H., 2012. Accurate solution to diffraction around a modified v-shaped breakwater. *Coast. Eng.* 68, 56–66.
- Chen, Q., Zang, J., Birchall, J., Ning, D.Z., Zhao, X.L., Gao, J.L., 2020. On the hydrodynamic performance of a vertical pile-restrained WEC-type floating breakwater. *Renew. Energy* 146, 414–425.
- Chen, Z.J., Wang, Y.X., Dong, H.Y., Zheng, B.X., 2012. Time-domain hydrodynamic analysis of pontoon-plate floating breakwater. *Water Sci. Eng.* 5 (3), 291–303.
- Cheng, Y., Du, W.M., Dai, S.S., Ji, C.Y., Collu, M., Cocard, M., Cui, L., Yuan, Z., Incecik, A., 2022. Hydrodynamic characteristics of a hybrid oscillating water column-oscillating buoy wave energy converter integrated into a π -type floating breakwater. *Renew. Sustain. Energy Rev.* 161, 112299.
- Christensen, E.D., Bingham, H.B., Friis, A., Larsen, A.K., Jensen, K.L., 2018. An experimental and numerical study of floating breakwaters. *Coast. Eng.* 137, 43–58.
- Correia, F.X., Gomes, R.P.F., Henriques, J.C.C., Gato, L.M.C., Falcao, A.F.O., 2016. Model testing of an oscillating water column spar-buoy wave energy converter isolated and in array: motions and mooring forces. *Energy* 112, 1207–1218.
- Diamantoulaki, I., Angelides, D., 2010. Analysis of performance of hinged floating breakwaters. *Eng. Struct.* 32, 2407–2423.
- Elhanafi, A., Macfarlane, G., Ning, D.Z., 2018. Hydrodynamic performance of single-chamber and dual-chamber offshore-stationary Oscillating water Column devices using CFD. *Appl. Energy* 228, 82–96.
- Fossa, M., Guglielmini, G., 2002. Pressure drop and void fraction profiles during horizontal flow through thin and thick orifices. *Exp. Therm. Fluid Sci.* 26, 513–523.
- Goda, Y., Suzuki, Y., 1976. Estimation of incident and reflected waves in random wave experiments. In: *Proceedings of the 15th international conference on coastal engineering ASCE*, pp. 828–845.
- Guo, B.M., Ning, D.Z., Wang, R.Q., Ding, B.Y., 2021. Hydrodynamics of an oscillating water column WEC - breakwater integrated system with a pitching front-wall. *Renew. Energy* 176, 67–80.
- Howe, D., Nader, J.R., Macfarlane, G., 2020. Experimental investigation of multiple oscillating water column wave energy converters integrated in a floating breakwater: energy extraction performance. *Appl. Ocean Res.* 97, 102086.
- He, F., Huang, Z.H., Adrian, W.-K.L., 2013. An experimental study of a floating breakwater with asymmetric pneumatic chambers for wave energy extraction. *Appl. Energy* 106, 222–231.
- He, F., Zhang, H., Zhao, J., Zheng, S., Iglesias, G., 2019. Hydrodynamic performance of a pilesupported OWC breakwater: an analytical study. *Appl. Ocean Res.* 88, 326–340.
- International Energy Agency (IEA). *Renewables 2020 data explorer*. <https://www.iea.org/reports/clean-energy-transitions-programme-2020>.
- Ji, C.Y., Cheng, Y., Yang, K., Oleg, G., 2017. Numerical and experimental investigation of hydrodynamic performance of a cylindrical dual pontoon-net floating breakwater. *Coast. Eng.* 129, 1–16.
- Kramer, M., Marquis, L., Frigaard, P., 2011. Performance evaluation of the Wavestar prototype. In: *Proceedings of the 9th European Wave and Tidal Energy Conference (EWTEC)*. Southampton, UK.
- Koo, W., 2009. Nonlinear time-domain analysis of motion-restrained pneumatic floating breakwater. *Ocean Eng.* 36, 723–731.
- Liu, Z., Wang, Y., 2020. Numerical studies of submerged moored box-type floating breakwaters with different shapes of cross-section using SPH. *Coast. Eng.* 158, 103687.
- Liu, Y., Li, H.J., 2014. A new semi-analytical solution for gap resonance between twin rectangular boxes. *Proc. Inst. Mech. Eng. Part M: J. Eng. Marit Environ.* 228, 3–16.
- Liang, J.M., Liu, Y., Chen, Y.K., Li, A.J., 2022. Experimental study on hydrodynamic characteristic of the box-type floating breakwater with different mooring configurations. *Ocean Eng.* 254, 111296.
- Madhi, F., Yeung, R.W., 2018. On survivability of asymmetric wave-energy converters in extreme waves. *Renew. Energy* 119, 891–909.
- Michaelides, C., Angelides, D., 2012. Modeling of energy extraction and behavior of a flexible floating breakwater. *Appl. Ocean Res.* 35, 77–94.
- Ma, Q.W., Wu, G.X., Eatock, Taylor R., 2010. Finite element simulation of fully nonlinear interaction between vertical cylinders and steep waves. Part 1: methodology and numerical procedure. *Int. J. Numer. Methods Fluid.* 36, 265–285.
- Ning, D.Z., Zhao, X.L., Goteman, M., Kang, H.G., 2016a. Hydrodynamic performance of a pile-restrained WEC-type floating breakwater: an experimental study. *Renew. Energy* 95, 531–541.
- Ning, D.Z., Wang, R.Q., Zou, Q.P., Teng, B., 2016b. An experimental investigation of hydrodynamics of a fixed OWC wave energy converter. *Appl. Energy* 168, 636–648.
- Ning, D.Z., Zhao, X.L., Zhao, M., Hann, M., Kang, H.G., 2017. Analytical investigation of hydrodynamic performance of a dual pontoon WEC-type breakwater. *Appl. Ocean Res.* 65, 102–111.
- Ning, D.Z., Wang, R.Q., Chen, L.F., Sun, K., 2019. Experimental investigation of a land-based dual-chamber OWC wave energy converter. *Renew. Sustain. Energy Rev.* 105, 48–60.
- Oliveira-Pinto, S., Rosa-Santos, P., Taveira-Pinto, F., 2020. Assessment of the potential of combining wave and solar energy resources to power supply worldwide offshore oil and gas platforms. *Energy Convers. Manag.* 223, 113299.
- Pawitan, K., Dimakopoulos, A., Vicinanza, D., Allsop, W., Bruce, T., 2019. A loading model for an OWC caisson based upon large-scale measurements. *Coast. Eng.* 145, 1–20.
- Tang, H.J., Huang, C.C., Chen, W.M., 2011. Dynamics of dual pontoon floating structure for cage aquaculture in a two-dimensional numerical wave tank. *J. Fluid Struct.* 27, 918–936.
- Veer, R.V., Thorlen, H.J., 2008. Added resistance of moonpools in calm water. In: *Proceedings of the ASME 27th International Conference on Offshore Mechanics and Arctic Engineering*. Estoril, Portuga.
- Windt, C., Daidson, J., Ringwood, J.V., 2021. Numerical analysis of the hydrodynamic scaling effects for the Wavestar wave energy converter. *J. Fluid Struct.* 105, 103328.
- Wang, C., Ma, T., Zhang, Y.L., 2022. Semi-analytical study on an integrated-system with separated heaving OWC and breakwater: structure size optimization and gap resonance utilization. *Ocean Eng.* 245, 110319.
- Wei, P., Lee, K.H., Shin, S.H., Norimi, M., 2013. Numerical simulation of interactions between wave waves and inclined-moored submerged floating breakwaters. *Coast. Eng.* 82, 76–87.
- Zhang, H.M., Zhou, B.Z., Zang, J., Vogel, C., Fan, T.H., Chen, C.H., 2021a. Effects of narrow gap wave resonance on a dual-floater WEC-breakwater hybrid system. *Ocean Eng.* 225, 108762.
- Zhang, H.M., Zhou, B.Z., Zang, J., Vogel, C., Jin, P., Ning, D.Z., 2021b. Optimization of a three-dimensional hybrid system combining a floating breakwater and a wave energy converter array. *Energy Convers. Manag.* 247, 114717.
- Zhu, Q.Y., Chen, X.F., Song, M.L., Li, X.C., Shen, Z.Y., 2022. Impacts of renewable electricity standard and Renewable Energy Certificates on renewable energy investments and carbon emissions. *J. Environ. Manag.* 306, 114495.
- Zheng, S.M., Antonini, A., Zhang, Y.L., Greaves, D., Miles, J., Iglesias, G., 2019. Wave power extraction from multiple oscillating water columns along a straight coast. *J. Fluid Mech.* 878, 445–480.